

Analytical Reconstruction of Periodically Deformed Objects in Time-resolved CT

Qianwei Qu¹ Christian M. Schlepütz¹ Marco Stampanoni^{1,2}

¹Swiss Light Source, Paul Scherrer Institute, 5232 Villigen PSI, Switzerland

²Institute for Biomedical Engineering, University and ETH Zürich, Zurich, Switzerland

{qianwei.qu, christian.schlepuetz, marco.stampanoni}@psi.ch

Abstract

Time-resolved CT is an advanced measurement technique that has been widely used to observe dynamic objects, including periodically varying structures such as hearts, lungs, or hearing structures. To reconstruct these objects from CT projections, a common approach is to divide the projections into several collections based on their motion phases and perform reconstruction within each collection, assuming they originate from a static object. This describes the gating-based method, which is the standard approach for time-periodic reconstruction. However, the gating-based reconstruction algorithm only utilizes a limited subset of projections within each collection and ignores the correlation between different collections, leading to inefficient use of the radiation dose. To address this issue, we propose two analytical reconstruction pipelines in this paper, and validate them with experimental data captured using tomographic synchrotron microscopy. We demonstrate that our approaches significantly reduce random noise in the reconstructed images without blurring the sharp features of the observed objects. Equivalently, our methods can achieve the same reconstruction quality as gating-based methods but with a lower radiation dose. Our code is available at github.com/PeriodRecon.

1. Introduction

Computed Tomography (CT) is a widely used imaging technique that enables the reconstruction of cross-sectional images of an object from a series of projections taken at different angles [5, 20, 46]. It has revolutionized medical diagnostics [4, 24, 30, 37, 40], industrial inspection [6, 8, 10, 41], and scientific research [1, 13, 14, 31] by providing detailed and accurate three-dimensional visualization of internal structures. Traditional static CT assumes that the object being imaged remains motionless during the acquisition process. However, in many practical applications, objects exhibit motion or deformation, which introduces challenges, such as motion artifacts [21, 36, 49], and

degraded image quality.

To address these challenges, time-resolved CT, also known as dynamic CT, has emerged as a powerful extension of conventional CT [2]. Time-resolved CT captures temporal changes of an object during imaging, enabling the reconstruction of dynamic processes in addition to spatial information [34]. This capability is essential for imaging objects that undergo motion or deformation over time [3, 19].

A particularly significant category of dynamic CT problems involves objects undergoing cyclic motion or structural changes. This phenomenon is pervasive in both natural and engineered systems, making it a crucial area of study. For example, the periodic motion of the heart during cardiac cycles [37, 45] and the rhythmic expansion and contraction of the lungs during breathing [25, 35] serve as quintessential examples of periodic deformation. Beyond medical applications, CT is also employed in the investigation of other cyclic processes, such as materials subjected to compression-stretch fatigue loading [47] or low-strain vibration [29]. These studies enhance our understanding of how structures respond to repeated stress and deformation, contributing to advancements in both biomedical and material sciences.

To effectively image and analyze such periodic signals in dynamic CT, gating-based reconstruction algorithms have been widely employed. Gating techniques utilize external or internal signals to synchronize data acquisition with specific phases of periodic motion, as shown in Fig. 1(a), thereby mitigating motion artifacts and improving reconstruction accuracy. For example, in cardiac CT, electrocardiogram (ECG)-gating [9] is used to acquire projection data at consistent phases of the heart cycle, allowing for clear imaging of the beating heart. Similarly, in respiratory-gated CT [45], external or internal sensors detect the breathing cycle to reconstruct images at specific phases of lung motion. These techniques ensure that periodic deformation is captured in a controlled and phase-resolved manner, enabling more accurate reconstructions.

In dynamic CT, the camera exposure time must be sufficiently short to avoid motion artifacts. Additionally, the

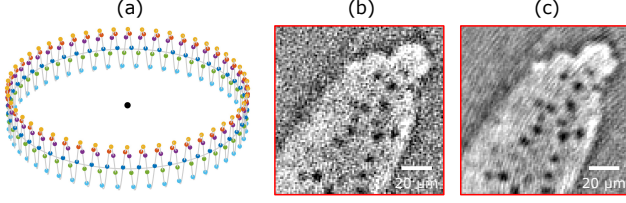


Figure 1. (a) Illustration of the gating process. Projections acquired at the same phase of the dynamic object (represented by points of the same color) are treated as if they were captured from a static object. (b) Reconstructed image using the gating-based algorithm. The structure depicted is a fish bone, imaged with synchrotron radiation. (c) Reconstructed image generated using the algorithm proposed in this study. The image quality is significantly enhanced, preserving sharp shape features while avoiding blurring (the edge of the bone and the black holes within the bone remain well-defined).

X-ray dose must be limited to prevent damage to the targets. Both factors result in a decrease in the number of photons arriving at the detectors. As a consequence, images obtained in dynamic CT scans are easily affected by random noise. Although the gating-based method efficiently mitigates motion artifacts in CT reconstructions, it overlooks the correlation between different phases, limiting its ability to fully leverage projection data for enhancing the quality of reconstructed images, as shown in Fig. 1(b). Especially, small grayscale changes due to pixel or sub-pixel scale motion may be easily buried in random noise.

In this paper, we propose two analytical methods to reconstruct time-periodic distributions, which are validated using real experimental data, as shown in Fig. 1(c). Both methods efficiently compress random noise in reconstructed images. As analytical algorithms, they are computationally efficient and theoretically interpretable, making them applicable to high-resolution dynamic CT scans.

2. Related works - Gating-based CT

Gating-based CT addresses the limitation of requiring a static object during CT by synchronizing data acquisition with specific phases of periodic motion and efficiently removing the motion artifacts when reconstructing periodically varying objects.

The ECG-gated CT is a typical medical application of gating-based method. This technique calculates the phase of heart beating from electrocardiograms (ECG) as the gating reference in cardiac CT scans. See the review by Desjardins and Kazerooni [9] and the references therein for more details.

Breathing signals are used for lung PET(positron emission tomography)/CT scans to reduce the motion artifacts. The reference signal can be recorded via external markers placed on the thorax [35] or by extracting the breathing

signal from the projection data [18]. Feng *et al.* proposed an adaptive center-of-mass approach for respiratory gating [12]. Walker *et al.* claims that the data-driven respiratory gating outperforms the device-based gating for clinical ^{18}F -FDG PET/CT [43].

The gating-based method are also used in the reconstruction of other biomechanical systems. Walker *et al.* [44] detect the wing beat pattern of a blowfly with 4D CT, where the gating signal is derived from spatial cross-correlation of successive projections[32]. Cercos-Pita *et al.* investigated lung tissue biomechanics in live rats where retrospective gating methodology was used to reconstruct 4D CT images [7]. Schmeltz *et al.* investigated the dynamic response of human auditory structures using the stimulating sound pattern as the gating reference [38].

In material sciences, gated-CT has been applied to analyze vibrating mechanical components and cyclic deformations in materials. For instance, stroboscopic techniques combined with X-ray CT have enabled the visualization of cyclic processes like compression-tension tests [29, 47].

In addition to classical gating techniques, improved methods have been proposed as well. For instance, Hermann *et al.* introduced a frequency-selective CT reconstruction technique capable of imaging both low- and high-frequency dynamic periodic motion [17], while Zhang *et al.* compared various attenuation correction methods for dual-gating myocardial perfusion SPECT/CT [48]. Klos *et al.* focused on enhancing the performance of retrospective gated-CT through numerical simulations and experimental validations [23]. By coupling vibration testing with tomographic simulations of particles with known geometries, they demonstrated methods to achieve uniform angular sampling and reduce motion artifacts at oscillation frequencies up to 400 Hz.

In summary, gating-based CT has become an essential tool for imaging periodically deformed objects in medical, biological, and industrial applications. Its flexibility and robustness make it well-suited for capturing high-frequency periodic signals with improved spatial and temporal resolutions. However, the method ignores the correlation between different phases, and thus cannot fully exploit the projection data to improve the quality of reconstructed images.

3. Method

3.1. Forward problem

We consider a well-defined, time-periodic distributed function $f(x, y, \varphi)$, where φ is the temporal phase of this dynamic field. Then, the function can be expanded using a

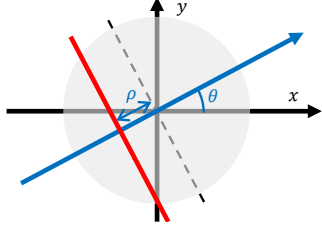


Figure 2. Geometry of the projection transform. The red line indicates the direction of the X-ray, *i.e.* the integration direction of the projection operator. The variable θ represents the rotational angle respective to the spatial x -axis; ρ denotes the shift of the X-ray from center (indicated by the dash line).

Fourier series:

$$f(x, y, \varphi) = a_0(x, y) + \sum_{k=1}^{\infty} a_k(x, y) \cos(k\varphi) + \sum_{k=1}^{\infty} b_k(x, y) \sin(k\varphi). \quad (1)$$

The Radon transform of the function is

$$\begin{aligned} p(\rho, \theta, \varphi) &= \mathcal{R}[f(x, y, \varphi); \rho, \theta] \\ &= \int_{-\infty}^{+\infty} \int_{-\infty}^{+\infty} f(x, y, \varphi) \\ &\quad \times \delta(x \cos \theta + y \sin \theta - \rho) \, dx \, dy, \end{aligned} \quad (2)$$

where $\delta(\cdot)$ is the Dirac-Delta function and the meanings of θ and ρ are illustrated in Fig. 2. Applying the Radon projection transform to $f(x, y, \varphi)$ with respect to the spatial components, and considering that the Radon transform is both linear and independent of φ , we derive that:

$$p(\rho, \theta, \varphi) = \mathcal{R}[a_0(x, y); \rho, \theta] \quad (3)$$

$$+ \sum_{k=1}^{\infty} \mathcal{R}[a_k(x, y); \rho, \theta] \cos(k\varphi) \quad (4)$$

$$+ \sum_{k=1}^{\infty} \mathcal{R}[b_k(x, y); \rho, \theta] \sin(k\varphi), \quad (5)$$

Let

$$p_k(\rho, \theta) = \mathcal{R}[a_k(x, y); \rho, \theta], \quad (6)$$

$$q_k(\rho, \theta) = \mathcal{R}[b_k(x, y); \rho, \theta], \quad (7)$$

then

$$p(\rho, \theta, \varphi) = p_0(\rho, \theta) + \sum_{k=1}^{\infty} p_k(\rho, \theta) \cos(k\varphi) \quad (8)$$

$$+ \sum_{k=1}^{\infty} q_k(\rho, \theta) \sin(k\varphi). \quad (9)$$

3.2. Inverse problem

3.2.1. Reconstruction with a lock-in amplifier (LIA)

If $p_k(\rho, \theta)$ and $q_k(\rho, \theta)$ are separated from $p(\rho, \theta, \varphi)$, we can first reconstruct $a_k(x, y)$ and $b_k(x, y)$ and subsequently retrieve $f(x, y, \varphi)$ using the linear combination shown in Eq. (1). Specifically, by taking the Fourier transform of $p(\rho, \theta, \varphi)$ with respect to ρ , denoted as $P(\omega, \theta, \varphi)$, we obtain:

$$P(\omega, \theta, \varphi) = P_0(\omega, \theta) + \sum_{k=1}^{\infty} P_k(\omega, \theta) \cos(k\varphi) \quad (10)$$

$$+ \sum_{k=1}^{\infty} Q_k(\omega, \theta) \sin(k\varphi), \quad (11)$$

where P_k and Q_k are the Fourier transforms of $p_k(\rho, \theta)$ and $q_k(\rho, \theta)$, respectively. Recalling the central slice theorem and the filtered back-projection algorithm [5], the following equation holds:

$$a_k(x, y) = \int_0^\pi \hat{p}_k(\rho, \theta)|_{\rho=x \cos \theta + y \sin \theta} \, d\theta, \text{ for } k = 0, 1, \dots, \quad (12)$$

$$b_k(x, y) = \int_0^\pi \hat{q}_k(\rho, \theta)|_{\rho=x \cos \theta + y \sin \theta} \, d\theta, \text{ for } k = 1, 2, \dots, \quad (13)$$

where $\hat{p}_k(\rho, \theta)$ and $\hat{q}_k(\rho, \theta)$ are the inverse Fourier transforms of $|\omega|P_k(\omega, \theta)$ and $|\omega|Q_k(\omega, \theta)$, respectively.

The separation of $p_k(\rho, \theta)$ and $q_k(\rho, \theta)$ can be achieved using the lock-in amplification theory [22, 39]. For in-

stance, consider the cosine part:

$$\begin{aligned} p(\rho, \theta, \varphi) \cos(m\varphi) \\ = p_0(\rho, \theta) \cos(m\varphi) \\ + \sum_{k=1}^{\infty} p_k(\rho, \theta) \cos(m\varphi) \cos(k\varphi) \end{aligned} \quad (14)$$

$$\begin{aligned} + \sum_{k=1}^{\infty} q_k(\rho, \theta) \sin(k\varphi) \cos(m\varphi) \\ = p_0 \cos(m\varphi) \end{aligned} \quad (15)$$

$$+ \frac{1}{2} \sum_{k=1}^{\infty} p_k(\rho, \theta) \cos(k\varphi + m\varphi) \quad (16)$$

$$+ \frac{1}{2} p_m(\rho, \theta) \quad (17)$$

$$+ \frac{1}{2} \sum_{\substack{k=1, \\ k \neq m}}^{\infty} p_k(\rho, \theta) \cos(k\varphi - m\varphi) \quad (18)$$

$$+ \frac{1}{2} \sum_{k=1}^{\infty} q_k(\rho, \theta) \sin(k\varphi + m\varphi) \quad (19)$$

$$+ \frac{1}{2} \sum_{k=1}^{\infty} q_k(\rho, \theta) \sin(k\varphi - m\varphi), \quad (20)$$

where $p_m(\rho, \theta)$ can be extracted using a lower-pass filter. In this equation, the products of $p(\rho, \theta, \varphi)$ with trigonometric functions shift its spectrum. By varying m and repeating the procedure for both cosine and sine components, we can calculate all $p_k(\rho, \theta)$ and $q_k(\rho, \theta)$ and subsequently, reconstruct $a_k(x, y)$ and $b_k(x, y)$.

Note that we must handle $p_0(\rho, \theta)$ with care. The high-frequency components of $P(\omega, \theta, \varphi)$ contain spatial details of the imaging area. Therefore, one cannot use a low-pass filter to extract p_0 from $p(\rho, \theta, \varphi)$. Instead, p_0 can be calculated by subtracting the other harmonics from $p(\rho, \theta, \varphi)$, i.e.

$$\begin{aligned} p_0(\rho, \theta) = p(\rho, \theta, \varphi) - \sum_{k=1}^{\infty} p_k(\rho, \theta) \cos(k\varphi) \\ - \sum_{k=1}^{\infty} q_k(\rho, \theta) \sin(k\varphi). \end{aligned} \quad (21)$$

Then, we have

$$a_0(x, y) = \int_0^{\pi} \hat{p}_0(\rho, \theta) |_{\rho=x \cos \theta + y \sin \theta} d\theta. \quad (22)$$

In the following section, we demonstrate that this step can be streamlined by more concise calculations.

With all reconstructed $a_k(x, y)$ and $b_k(x, y)$, we retrieve $f(x, y, \varphi)$ through a linear combination (Eq. (1)). Figure 3 illustrates the flowchart of the LIA-based reconstruction pipeline.

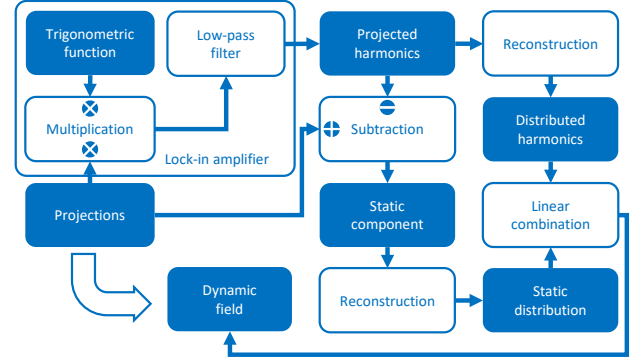


Figure 3. Flowchart of LIA-based reconstruction

3.2.2. Reconstruction with a frequency shifter (FS)

In Sec. 3.2.1, the harmonics p_k and q_k are separated using a lock-in amplifier, where a low-pass filter is required. In this section, we demonstrate how to eliminate this filter.

Retrieval of $a_0(x, y)$ First, we show that $a_0(x, y)$ can be directly reconstructed from $p(\rho, \theta, \varphi)$, thereby avoiding the need of Eq. (21) and (22), i.e.,

$$a_0(x, y) = \int_0^{\pi} \hat{p}(\rho, \theta, \varphi) |_{\rho=x \cos \theta + y \sin \theta} d\theta. \quad (23)$$

Define the inverse Fourier transform of $|\omega|P(\omega, \theta, \varphi)$ as $\hat{p}(\rho, \theta, \varphi)$, we have

$$\hat{p}(\rho, \theta, \varphi) = \hat{p}_0(\rho, \theta) + \sum_{k=1}^{\infty} \hat{p}_k(\rho, \theta) \cos(k\varphi) \quad (24)$$

$$+ \sum_{k=1}^{\infty} \hat{q}_k(\rho, \theta) \sin(k\varphi). \quad (25)$$

For simplicity, we write $\hat{p}(\rho, \theta, \varphi) |_{\rho=x \cos \theta + y \sin \theta}$ as $\hat{p}(\theta, \varphi)$, $\hat{p}_k(\rho, \theta) |_{\rho=x \cos \theta + y \sin \theta}$ as $\hat{p}_k(\theta)$, and $\hat{q}_k(\rho, \theta) |_{\rho=x \cos \theta + y \sin \theta}$ as $\hat{q}_k(\theta)$, respectively. Since

$$a_0(x, y) = \int_0^{\pi} \hat{p}_0(\theta) d\theta,$$

the aim is equivalent to proving that

$$\begin{aligned} 0 = \sum_{k=1}^{\infty} \int_0^{\pi} \hat{p}_k(\theta) \cos(k\varphi) d\theta \\ + \sum_{k=1}^{\infty} \int_0^{\pi} \hat{q}_k(\theta) \sin(k\varphi) d\theta. \end{aligned} \quad (26)$$

Here, if we assume that

$$\varphi = 2N\theta, N \in \mathbb{N}, \quad (27)$$

where N represents the number of periods of φ that occur as θ scans from 0 to π , we can prove a stronger condition: for each k

$$\begin{aligned} \int_0^\pi \hat{p}_k(\theta) \cos(k\varphi) d\theta &= \Delta_{\cos,k,N}, \\ \int_0^\pi \hat{q}_k(\theta) \sin(k\varphi) d\theta &= \Delta_{\sin,k,N}, \end{aligned} \quad (28)$$

where $\Delta_{\cos,k,N}$ and $\Delta_{\sin,k,N}$ are inevitable discrete errors due to finite number of projections.

The conclusion is trivial if φ is independent of θ . Unfortunately, actual CT systems typically include a rotational device, making φ a function of θ . The following derivation targets the nontrivial condition. For the cosine components:

$$\begin{aligned} &\int_0^\pi \hat{p}_k(\theta) \cos(k\varphi) d\theta \\ &= \frac{1}{2N} \int_0^{2N\pi} \hat{p}_k\left(\frac{\varphi}{2N}\right) \cos(\varphi) d\varphi \\ &= \frac{1}{2N} \sum_{n=0}^{N-1} \int_{2n\pi}^{2(n+1)\pi} \hat{p}_k\left(\frac{\varphi}{2N}\right) \cos(k\varphi) d\varphi \\ &= \frac{1}{2\pi} \int_0^{2\pi} \cos(k\psi) d\psi \sum_{n=0}^{N-1} \frac{\pi}{N} \hat{p}_k\left(\frac{\psi}{2N} + n\frac{\pi}{N}\right), \end{aligned} \quad (29)$$

where

$$\varphi = \psi + 2n\pi.$$

Note that

$$\sum_{n=0}^{N-1} \frac{\pi}{N} \hat{p}_k\left(\frac{\psi}{2N} + n\frac{\pi}{N}\right) \quad (30)$$

is a discrete form of

$$\int_0^\pi \hat{p}_k(\psi) d\psi = a_k(x, y).$$

Thus,

$$\begin{aligned} &\int_0^\pi \hat{p}_k(\theta) \cos(k\varphi) d\theta \\ &= \frac{1}{2\pi} \int_0^{2\pi} \cos(\psi) d\psi a_k(x, y) + \Delta_{\cos,k,N} \\ &= \Delta_{\cos,k,N}, \end{aligned} \quad (31)$$

where $\Delta_{\cos,k,N}$ is the discrete error of Eq. (30). In any real CT scan, we cannot obtain continuous projections with infinite angles. Discrete errors are inevitable.

Retrieval of $a_k(x, y)$ and $b_k(x, y)$ Then, if we repeat the procedure in the previous section, for $k = 1, 2, \dots$, we have

$$a_k(x, y) = \int_0^\pi \hat{p}_k(\theta) d\theta \quad (32)$$

$$= 2 \int_0^\pi \hat{p}(\theta, \varphi) \cos(k\varphi) d\theta, \quad (33)$$

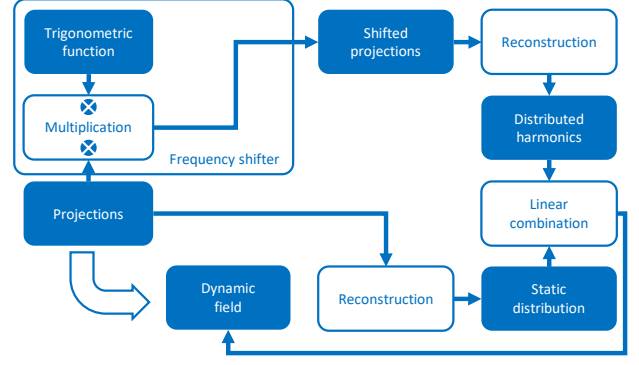


Figure 4. Flowchar of FS-based reconstruction

Similarly,

$$b_k(x, y) = 2 \int_0^\pi \hat{p}(\theta, \varphi) \sin(k\varphi) d\theta. \quad (34)$$

4. Experiment setup

As outlined in the preceding sections, our methods leverage projections extensively to enhance the quality of reconstructed images, aiming to achieve superior results compared to gating-based approaches. To demonstrate the effectiveness of our methods in real-world measurement environments, we validate them using experimental data.

The experimental setup is illustrated in Fig. 5 and explained in more detail in [26]. In this experiment, fish hearing structures were stimulated with sinusoidal sound waves, and their dynamic responses were investigated using synchrotron radiation, captured via tomographic microscopy. The experiment was conducted at the TOMCAT beamline of the Swiss Light Source, Paul Scherrer Institute.

5. Results and discussion

5.1. Reconstructed images

The images of dynamic fish hearing structures are reconstructed using our method and the standard gating-based method. Both methods employ the `gridrec` algorithm [11] implemented in the `tomopy` package [16]. In the gating-based reconstruction, all projections are grouped into 20 collections corresponding to the sound phases centered around 9, 27, 45, ..., 351 degrees. The synchrotron radiation can only scan a very small field of view, resulting in high spatial accuracy but also truncating the projections to a limited range compared with the entire fish cross-section. Therefore, we integrate the padding method [27, 28] into our pipeline to reduce local tomography artifacts.

The reconstructed images are compared in Fig. 6. The results demonstrate that our method efficiently reduces ran-

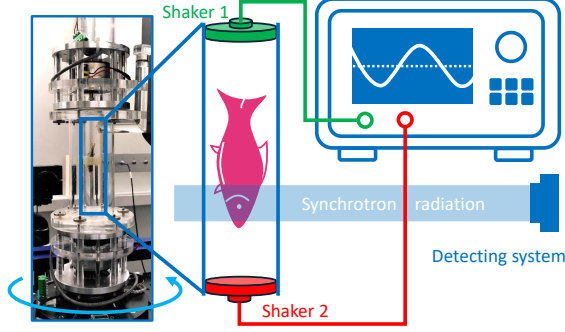


Figure 5. Experimental Setup. A *Sewellia lineolata* was placed inside a water-filled tube of a well-designed tank setup, as illustrated in the left panel. Two shakers, driven by 550 Hz signals from a sound generator, were positioned at both ends of the tube. The aquarium was placed on a rotation stage for tomographic data acquisition, rotating at a speed of 90 degrees per second and covering a range from 0 to 180 degrees in 2 seconds. Synchrotron X-ray radiation passing through the sample was captured by an imaging system consisting of a microscope and a high-speed camera [33] with an equivalent pixel size of $1.1 \times 1.1 \mu\text{m}^2$. The camera operated at a frame rate of 10 kfps, resulting in 20 000 projection images over the 2-second rotation period. The camera’s exposure signal was recorded with the same data acquisition card that was registering the sound stimulus signal, and the rotation angle read-back for each exposure was also recorded and saved.

dom noise without smoothing the sharp features of the observed structures. We selected a 100 by 100 pixel region from the background, marked by red boxes in Fig. 6, to calculate the noise level in the reconstructed images. The standard deviation (STD) values of the intensities corresponding to the 10 000 pixels are listed in Tab. 1. The STD values for the gating-based method are approximately twice those of our method.

The supplementary video provides a similar demonstration to Fig. 6, comparing the intensity differences at different sound phases.

The figures and tables indicate that our methods can efficiently reduce random noise levels in the reconstructed images. If the original signal-to-noise ratio is satisfactory, we can leverage this property to reduce radiation dose in experiments. To achieve this, two approaches are possible: (a) using shorter exposure times and then applying our methods to improve image quality; (b) using fewer projection angles. The results of the second approach are demonstrated in the supplementary materials.

5.2. LIA filter design

Figure 7 illustrates the Fourier transforms of the projection sequence of one pixel.

In the LIA-based method, zero-phase filtering [15] should be adopted to avoid signal shift in the time domain. The exposure timestamp corresponds to the projection an-

Table 1. Noise level comparison. The noise is sampled from the regions marked with blue boxes in Fig. 6. The standard deviation (STD) values of the intensities are listed in this table.

Row	Gating	LIA	FS
1	1.47×10^{-3}	6.29×10^{-4}	7.97×10^{-4}
2	1.45×10^{-3}	5.92×10^{-4}	7.73×10^{-4}
3	1.45×10^{-3}	5.93×10^{-4}	7.70×10^{-4}
4	1.46×10^{-3}	5.97×10^{-4}	7.73×10^{-4}
5	1.47×10^{-3}	5.94×10^{-4}	7.85×10^{-4}
6	1.44×10^{-3}	5.94×10^{-4}	7.66×10^{-4}

gle, and thus, a shift in the time domain rotates the reconstructed image. In our code, the zero-phase filtering is implemented based on the `sosfiltfilt` function implemented in the `scipy` package [42]. Finite impulse response filters have linear phase shifts which are easier to be compensated. We intentionally choose an infinite impulse response filter to expose the importance of phase shift compensation.

The filtering process generates transient responses at both ends of the sequence. To mitigate these effects, the 180-degree projections are initially extended to 360-degree ones and then truncated back to 180-degree projections after filtering. The phase plots in Fig. 7 show that the input and output signals maintain consistent phases in the pass-band. Zero-phase filters perform two passes (forward and backward), effectively resulting in a 12th-order filter, even though a 6th-order filter was designed.

5.3. Harmonics

The reconstructed static distribution, $a_0(x, y)$, and the harmonics, $a_k(x, y)$ and $b_k(x, y)$, using the FS-based method are shown in Fig. 8 (those of the LIA-based method are similar). We truncated the Fourier series at the second harmonics, as higher harmonics contribute little to the total signal energy. It is important to note that $a_0(x, y)$ does not represent a static distribution when the structures are motionless. Instead, the physically static state, *i.e.*, without stimulation, corresponds to a dynamic distribution at a specific time point.

The base tones a_1 and b_1 dominate the energy of the dynamic part. Stronger variations are observed on the edge of the stimulated scaphium compared to other structures. The motion of the scaphium also generates second-order harmonics in a_2 and b_2 , whereas those of the other bones are indistinguishable from the background.

5.4. Dynamic distributions

Our method calculates the dynamic distribution at any given time. Although the gating-based method can achieve similar results by sliding the gating window, the phases are less

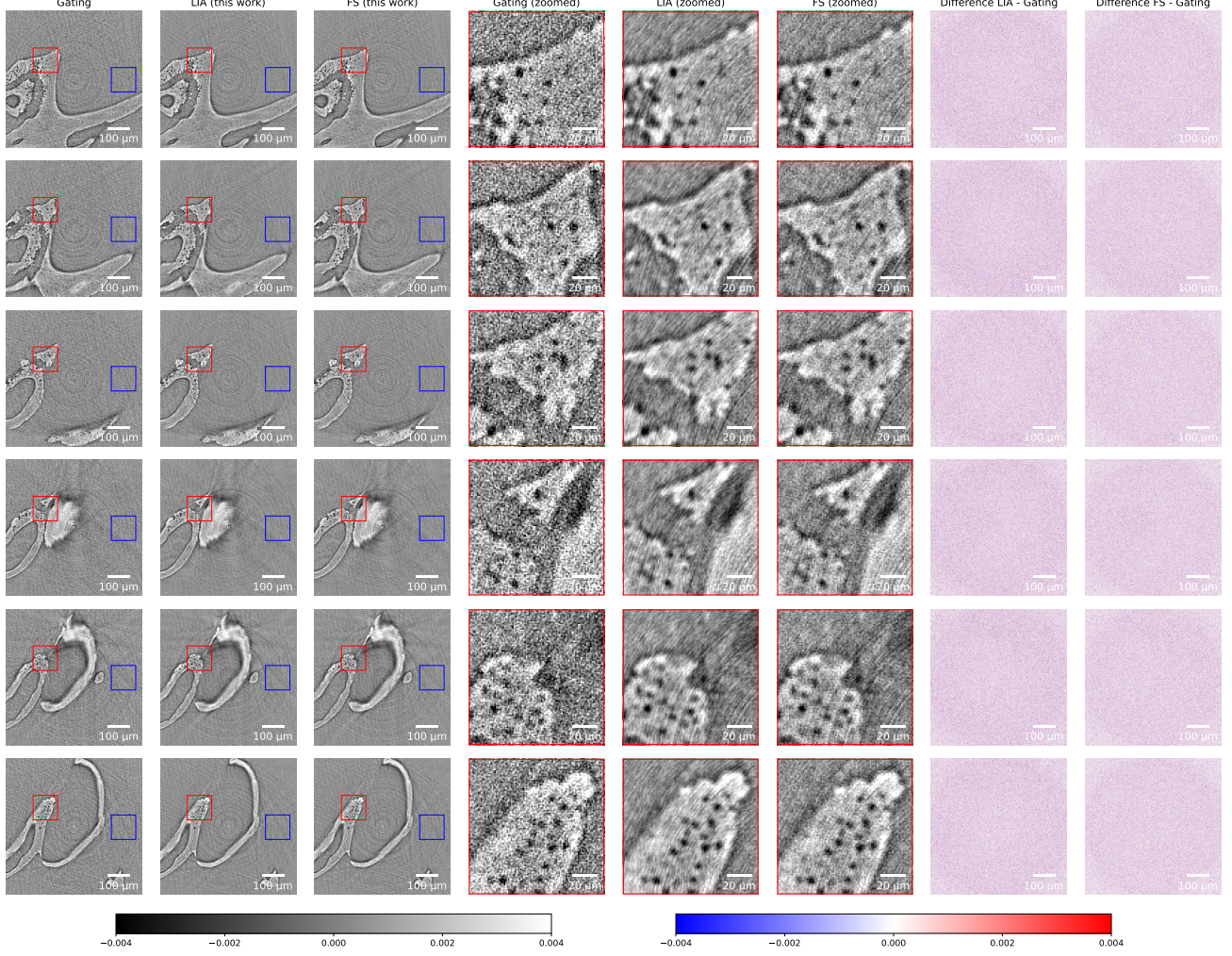


Figure 6. Reconstruction quality comparison for the sound phase of 9 degrees. The figure compares the reconstructed slices obtained using the gating-based method (first column) and our methods (second and third columns). For our methods, we utilize the harmonics of the first two orders, *i.e.*, $k = 1, 2$, to retrieve the dynamic distributions. In these images, the crescent-moon-like structure represents the scaphium of the fish, expected to be stimulated by the sound wave; other bones are anticipated to remain static but may exhibit slight vibrations during the experiment. The fourth to the sixth columns are the blow-ups of the red boxes regions in the first three columns, respectively. The last two columns show the intensity differences between the images in the first three columns.

accurate. The sound phases (φ) at camera exposures are shown in Fig. 9. Projections nominally corresponding to the 9-degree phase are actually collected from 0 to 18 degrees. In contrast, our method calculates the dynamic distributions at exactly 9 degrees. In this experiment, the gating-based method and our method show no observable difference, but the difference can be significant in cases with larger motion.

5.5. Noise reduction

Our method reduces the noise energy in two aspects. First, the frequency shifter separates the time-invariant components from the projections without decreasing the number of projections, and all of them are fed to the reconstruction

program. In contrast, only a small fraction of the projections (1/20 in our case) can be used in the gating-based reconstruction. The LIA enables us to utilize the correlations among frames to reduce random noise, analogous to a mean filter. However, when we increase the harmonics used in the final linear combination, we introduce additional noise.

Secondly, the lock-in amplifier (LIA) extracts the signal and compresses random noise. In the Fourier domain, periodic signals have a sparse representation, making them easily distinguishable from noise.

Figure 10 plots the noise levels as a function of the highest order of harmonics and the cutoff frequency used in the LIA-based method.

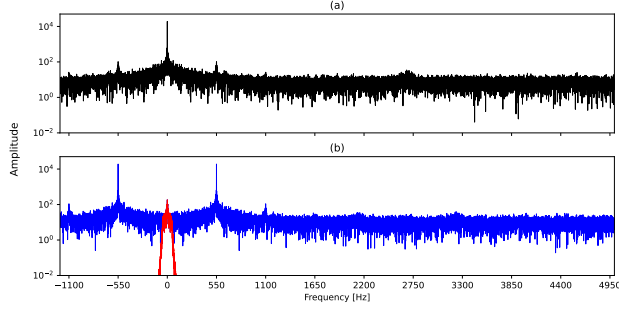


Figure 7. (a) The magnitude of the Discrete Fourier Transform (DFT) of the original projection sequence at the 206-th pixel, corresponding to the last slice in Fig. 6. (b) The blue curve is the magnitude of the DFT of the product between the sequence and $\cos(1\varphi)$, while the red curve shows the output after passing the product through a low-pass filter with a cutoff frequency of 50 Hz.

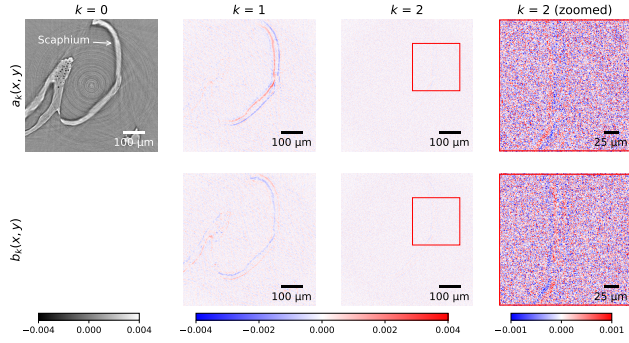


Figure 8. Reconstructed $a_k(x, y)$ and $b_k(x, y)$ using the FS-based algorithm.

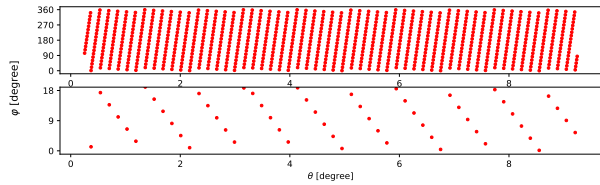


Figure 9. (a) The fitted sound phases of the first 1000 sampling points out of the 20 000 ones. (b) A blow-up of the first collection of the gating procedure, with the nominal phase of 9 degrees.

5.6. Applicable scenarios

Both our methods are applicable to the reconstruction of time-periodic fields either for improving the signal-noise ratio or equivalently decreasing the radiation dose.

The lock-in amplifier is a plug-in element that can be integrated with any reconstruction algorithm, although this work uses an analytical algorithm. In contrast, the derivation in Sec. 3.2.2 relies on the central slice theorem. While we cannot prove the applicability of the FS-based method to all reconstruction algorithms by enumeration, Eq. (29) rep-

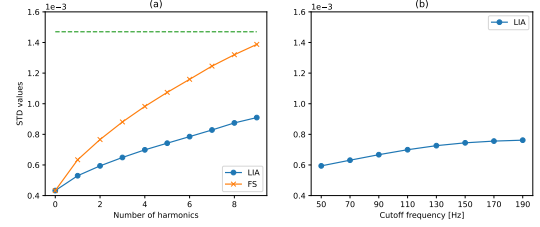


Figure 10. (a) Noise levels vary with the highest order of harmonics. The lock-in amplifier's cutoff frequency is set to 50 Hz. The green dashed line indicates the STD values corresponding to the gating-based algorithm. (b) Noise levels change with the cutoff frequency in the LIA-based method, where the highest order of harmonics is 2.

resents a regrouping operation, *i.e.*, the gating procedure, which can be performed before Fourier transformation and ramp filtering. Therefore, we are confident that the frequency shifter can also serve as a plug-in element for other reconstruction algorithms.

The FS-based algorithm is fast and easy to parallelize. Thus, it can potentially be integrated into real-time reconstruction pipelines. Although the low-pass filter slows down the LIA-based algorithm, it remains easy to parallelize and can be further accelerated using mature signal processing techniques, such as Fast-Fourier-Transform filtering. However, the LIA-based algorithm is primarily designed for post-processing, even if speed is not an issue, because the lock-in amplifier's filter typically needs to be tuned to achieve optimal image quality. In this work, we use a global bandwidth, filter type, and filter order for all projection sequences, which is not necessary. A smart strategy could be developed to adaptively determine these super-parameters, a topic that warrants further investigation.

Our method effectively compresses random noise, but it does not reduce static artifacts. For instance, noticeable ring artifacts are present in the static distribution shown in Fig. 8 and are subsequently introduced into the dynamic distributions in Fig. 6. However, the increased contrast between the rings and the objects/background may benefit artifact reduction algorithms [28] that primarily operate in the spatial domain. Moreover, our method makes it feasible to apply these algorithms to the static component, avoiding potential negative effects on the dynamic harmonics. These findings warrant further investigation.

6. Conclusion

In this paper, we propose two analytical methods for reconstruction of periodically deformed objects. The LIA-based one extracts projected harmonics p_k and q_k from the time-resolved projections and reconstructs distributed harmonics a_k and b_k . In contrast, the FS-based method directly reconstructs the distributed harmonics from the time-resolved

projections.

Both methods maximize the use of projections and efficiently compress the random noise in the reconstructed images (or equivalently, achieve a similar signal-to-noise ratio with lower radiation dose compared to the gating-based approach). The performances of our methods surpasses that of the gating-based approach when applied to experimental data obtained in the observation of sound-stimulated fish hearing structures using synchrotron radiation.

Both methods have solid theoretical foundations and are computationally efficient, making them suitable for fast reconstruction in high-resolution 4D CT scans. Due to the presence of a low-pass filter, the LIA-based method is slower than the FS-based one, but offers superior noise reduction. The FS-based approach is particularly applicable to real-time reconstruction due to its lack of fine-tuned parameters.

Acknowledgement

We thank Isabelle P. Maiditsch, Tanja Schulz-Mirbach and Martin Heß (Ludwig Maximilian University of Munich) for implementing the experiment setup and preparing the sample.

We thank Federica Marone (Paul Scherrer Institute) for invaluable discussions.

We acknowledge the Paul Scherrer Institute, Villigen 5232, Switzerland, for provision of synchrotron radiation beamtime at the TOMCAT beamline X02DA of the SLS.

The project is funded by the Swiss National Science Foundation (310030E 205380).

References

- [1] Hassan Bahaloo, Fredrik Forsberg, Johan Casselgren, Henrik Lycksam, and Mikael Sjö Dahl. Mapping of density-dependent material properties of dry manufactured snow using μ CT. *Applied Physics A*, 130(1):16, 2024. 1
- [2] S. Bonnet, A. Koenig, S. Roux, P. Hugonnard, R. Guillemaud, and P. Grangeat. Dynamic X-ray computed tomography. *Proceedings of the IEEE*, 91(10):1574–1587, 2003. 1
- [3] Zachary V. Braig, Lauren E. Dittman, Kimberly K. Amrami, and Sanjeev Kakar. Dynamic Computed Tomography of the Distal Radioulnar Joint Versus Magnetic Resonance Imaging in Detecting Foveal Tears of the Triangular Fibrocartilage Complex. *HAND*, page 15589447241232012, 2024. 1
- [4] Matthew J. Budoff, Jerold S. Shinbane, Stephan Achenbach, Paolo Raggi, and John A. Rumberger, editors. *Cardiac CT Imaging*. Springer London, 2006. 1
- [5] Thorsten M. Buzug. Computed Tomography. In *Springer Handbook of Medical Technology*, pages 311–342. Springer Berlin Heidelberg, Berlin, Heidelberg, 2011. 1, 3
- [6] Simone Carmignato. Accuracy of industrial computed tomography measurements: Experimental results from an international comparison. *CIRP Annals*, 61(1):491–494, 2012. 1
- [7] Jose-Luis Cercos-Pita, Luca Fardin, Hugo Leclerc, Bertrand Maury, Gaetano Perchiazzi, Alberto Bravin, and Sam Bayat. Lung tissue biomechanics imaged with synchrotron phase contrast microtomography in live rats. *Scientific Reports*, 12(1):5056, 2022. 2
- [8] L. De Chiffre, S. Carmignato, J.-P. Kruth, R. Schmitt, and A. Weckenmann. Industrial applications of computed tomography. *CIRP Annals*, 63(2):655–677, 2014. 1
- [9] Benoit Desjardins and Ella A. Kazerooni. ECG-Gated Cardiac CT. *American Journal of Roentgenology*, 182(4):993–1010, 2004. 1, 2
- [10] Wim Dewulf, Harald Bosse, Simone Carmignato, and Richard Leach. Advances in the metrological traceability and performance of X-ray computed tomography. *CIRP Annals*, 71(2):693–716, 2022. 1
- [11] Betsy A. Dowd, Graham H. Campbell, Robert B. Marr, Vivek V. Nagarkar, Sameer V. Tipnis, Lisa Axe, and D. P. Siddons. Developments in synchrotron x-ray computed microtomography at the National Synchrotron Light Source. In *Developments in X-Ray Tomography II*, pages 224–236, Denver, CO, 1999. 5
- [12] Tao Feng, Jizhe Wang, Youjun Sun, Wentao Zhu, Yun Dong, and Hongdi Li. Self-Gating: An Adaptive Center-of-Mass Approach for Respiratory Gating in PET. *IEEE Transactions on Medical Imaging*, 37(5):1140–1148, 2018. 2
- [13] Daniel P. Glavin, Scott A. Eckley, José C. Aponte, Eve L. Berger, Aaron S. Burton, Jason P. Dworkin, Jamie E. Elsil, Frank T. Ferguson, Yoshihiro Furukawa, Heather V. Graham, Toshiaki Koga, Michael Liss, Hannah L. McLain, Hiroshi Naraoka, Yasuhiro Oba, Eric T. Parker, Kevin Richter, Philippe Schmitt-Kopplin, Danielle N. Simkus, Yoshinori Takano, Harold C. Connolly, and Dante S. Lauretta. Investigating the impact of x-ray computed tomography imaging on soluble organic matter in the Murchison meteorite: Implications for Bennu sample analyses. *Meteoritics & Planetary Science*, 59(1):105–133, 2024. 1
- [14] Federico Greco, Andrea Panunzio, Alessandro Tafuri, Caterina Bernetti, Vincenzo Pagliarulo, Bruno Beomonte Zobel, Arnaldo Scardapane, and Carlo Augusto Mallio. CT-Based Radiogenomics of P4HA3 Expression in Clear Cell Renal Cell Carcinoma. *Academic Radiology*, 31(3):902–908, 2024. 1
- [15] F. Gustafsson. Determining the initial states in forward-backward filtering. *IEEE Transactions on Signal Processing*, 44(4):988–992, 1996. 6
- [16] Doga Gürsoy, Francesco De Carlo, Xianghui Xiao, and Chris Jacobsen. TomoPy: a framework for the analysis of synchrotron tomographic data. *Journal of Synchrotron Radiation*, 21(5):1188–1193, 2014. 5
- [17] Jacob Herrmann, Eric A. Hoffman, and David W. Kaczka. Frequency-Selective Computed Tomography: Applications During Periodic Thoracic Motion. *IEEE Transactions on Medical Imaging*, 36(8):1722–1732, 2017. 2
- [18] Geoffrey D. Hugo and Mihaela Rosu. Advances in 4D radiation therapy for managing respiration: Part I – 4D imaging. *Zeitschrift für Medizinische Physik*, 22(4):258–271, 2012. 2

- [19] Thien J. Huynh, Donna Parizadeh, Ahmed K. Ahmed, Christopher T. Gandia, Hal C. Davison, John V. Murray, Ian T. Mark, Ajay A. Madhavan, Darya Shlapak, Todd D. Rozen, Waleed Brinjikji, Prasanna Vibhute, Vivek Gupta, Kacie Brewer, and Olga Fermo. Lateral Decubitus Dynamic CT Myelography with Real-Time Bolus Tracking (dCTM-BT) for Evaluation of CSF-Venous Fistulas: Diagnostic Yield Stratified by Brain Imaging Findings. *American Journal of Neuroradiology*, 45(1):105–112, 2024. 1
- [20] Willi A Kalender. X-ray computed tomography. *Physics in Medicine and Biology*, 51(13):R29–R43, 2006. 1
- [21] Kevin Kalisz, Ji Buethe, Sachin S. Saboo, Suhny Abbata, Sandra Halliburton, and Prabhakar Rajiah. Artifacts at Cardiac CT: Physics and Solutions. *RadioGraphics*, 36(7):2064–2083, 2016. 1
- [22] Kaushal Kishore and S. A. Akbar. Evolution of Lock-In Amplifier as Portable Sensor Interface Platform: A Review. *IEEE Sensors Journal*, 20(18):10345–10354, 2020. 3
- [23] Antoine Klos, Lucie Bailly, Sabine Rolland Du Roscoat, Laurent Orgéas, Nathalie Henrich Bernardoni, Ludovic Broche, and Andrew King. Optimising 4D imaging of fast-oscillating structures using X-ray microtomography with retrospective gating. *Scientific Reports*, 14(1), 2024. Publisher: Springer Science and Business Media LLC. 2
- [24] Naveen M. Kulkarni, Alice Fung, Avinash R. Kambadakone, and Benjamin M. Yeh. Computed Tomography Techniques, Protocols, Advancements, and Future Directions in Liver Diseases. *Magnetic Resonance Imaging Clinics of North America*, 29(3):305–320, 2021. 1
- [25] F Lamare, A Bousse, K Thielemans, C Liu, T Merlin, H Fayad, and D Visvikis. PET respiratory motion correction: quo vadis? *Physics in Medicine & Biology*, 67(3):03TR02, 2022. 1
- [26] Isabelle P. Maiditsch, Friedrich Ladich, Martin Heß, Christian M. Schlepütz, and Tanja Schulz-Mirbach. Revealing sound-induced motion patterns in fish hearing structures in 4D: a standing wave tube-like setup designed for high-resolution time-resolved tomography. *Journal of Experimental Biology*, 225(1):jeb243614, 2022. 5
- [27] F. Marone and M. Stampanoni. Regridding reconstruction algorithm for real-time tomographic imaging. *Journal of Synchrotron Radiation*, 19(6):1029–1037, 2012. 5
- [28] Federica Marone, Beat Münch, and Marco Stampanoni. Fast reconstruction algorithm dealing with tomography artifacts. In *Developments in X-Ray Tomography VII*, page 780410, San Diego, California, USA, 2010. 5, 8
- [29] Masami Matsubara, Taichi Komatsu, Ryo Takara, Masakazu Kobayashi, Shogo Furuta, Kentaro Uesugi, Asahi Nagatani, Shozo Kawamura, and Daiki Tajiri. Dynamic observation of a damping material using micro X-ray computed tomography coupled with a phase-locked loop. *Polymer Testing*, 117:107810, 2023. 1, 2
- [30] Joseph Maytal, Joel M. Krauss, Gerald Novak, Joy Nagelberg, and Mahindra Patel. The Role of Brain Computed Tomography in Evaluating Children with New Onset of Seizures in the Emergency Department. *Epilepsia*, 41(8):950–954, 2000. 1
- [31] M. Mijum, B. J. Andrews, T. J. McCoy, C. M. Corrigan, M. W. Caffee, and M. M. Tremblay. Using X-ray computed microtomography (μ CT) to determine subsample-specific cosmogenic noble gas production rates of E (enstatite) chondrites. *Meteoritics & Planetary Science*, page maps.14309, 2025. 1
- [32] Rajmund Mokso, Daniel A. Schwyn, Simon M. Walker, Michael Doube, Martina Wicklein, Tonya Müller, Marco Stampanoni, Graham K. Taylor, and Holger G. Krapp. Four-dimensional in vivo X-ray microscopy with projection-guided gating. *Scientific Reports*, 5(1):8727, 2015. 2
- [33] Rajmund Mokso, Christian M. Schlepütz, Gerd Theidel, Heiner Billich, Elmar Schmid, Tine Celcer, Gordan Mikuljan, Leonardo Sala, Federica Marone, Nick Schlumpf, and Marco Stampanoni. GigaFRoST: the gigabit fast readout system for tomography. *Journal of Synchrotron Radiation*, 24(6):1250–1259, 2017. 6
- [34] Beat Münch. Spatiotemporal computed tomography of dynamic processes. *Optical Engineering*, 50(12):123201, 2011. 1
- [35] S. A. Nehmeh, Y. E. Erdi, T. Pan, E. Yorke, G. S. Mageras, K. E. Rosenzweig, H. Schoder, H. Mostafavi, O. Squire, A. Pevsner, S. M. Larson, and J. L. Humm. Quantitation of respiratory motion during 4D-PET/CT acquisition. *Medical Physics*, 31(6):1333–1338, 2004. 1, 2
- [36] Medhat M. Osman, Christian Cohade, Yuji Nakamoto, and Richard L. Wahl. Respiratory motion artifacts on PET emission images obtained using CT attenuation correction on PET-CT. *European Journal of Nuclear Medicine and Molecular Imaging*, 30(4):603–606, 2003. 1
- [37] W T Roberts, J J Bax, and L C Davies. Cardiac CT and CT coronary angiography: technology and application. *Heart*, 94(6):781–792, 2008. 1
- [38] Margaux Schmeltz, Aleksandra Ivanovic, Christian M. Schlepütz, Wilhelm Wimmer, Aaron K. Remenschneider, Marco Caversaccio, Marco Stampanoni, Lukas Anschuetz, and Anne Bonnin. The human middle ear in motion: 3D visualization and quantification using dynamic synchrotron-based X-ray imaging. *Communications Biology*, 7(1):157, 2024. 2
- [39] John H. Scofield. Frequency-domain description of a lock-in amplifier. *American Journal of Physics*, 62(2):129–133, 1994. 3
- [40] I. Sluimer, A. Schilham, M. Prokop, and B. Van Ginneken. Computer analysis of computed tomography scans of the lung: a survey. *IEEE Transactions on Medical Imaging*, 25(4):385–405, 2006. 1
- [41] A Thompson, I Maskery, and R K Leach. X-ray computed tomography for additive manufacturing: a review. *Measurement Science and Technology*, 27(7):072001, 2016. 1
- [42] Pauli Virtanen, Ralf Gommers, Travis E. Oliphant, Matt Haberland, Tyler Reddy, David Cournapeau, Evgeni Burovski, Pearu Peterson, Warren Weckesser, Jonathan Bright, Stéfan J. Van Der Walt, Matthew Brett, Joshua Wilson, K. Jarrod Millman, Nikolay Mayorov, Andrew R. J. Nelson, Eric Jones, Robert Kern, Eric Larson, C J Carey, İlhan Polat, Yu Feng, Eric W. Moore, Jake VanderPlas, Denis Laxalde, Josef Perktold, Robert Cimman,

- Ian Henriksen, E. A. Quintero, Charles R. Harris, Anne M. Archibald, Antônio H. Ribeiro, Fabian Pedregosa, Paul Van Mulbregt, SciPy 1.0 Contributors, Aditya Vijaykumar, Alessandro Pietro Bardelli, Alex Rothberg, Andreas Hilboll, Andreas Kloeckner, Anthony Scopatz, Antony Lee, Ariel Rokem, C. Nathan Woods, Chad Fulton, Charles Masson, Christian Häggström, Clark Fitzgerald, David A. Nicholson, David R. Hagen, Dmitrii V. Pasechnik, Emanuele Olivetti, Eric Martin, Eric Wieser, Fabrice Silva, Felix Lenders, Florian Wilhelm, G. Young, Gavin A. Price, Gert-Ludwig Ingold, Gregory E. Allen, Gregory R. Lee, Hervé Audren, Irvin Probst, Jörg P. Dietrich, Jacob Silterra, James T Webber, Janko Slavič, Joel Nothman, Johannes Buchner, Johannes Kulick, Johannes L. Schönberger, José Vinícius De Miranda Cardoso, Joscha Reimer, Joseph Harrington, Juan Luis Cano Rodríguez, Juan Nunez-Iglesias, Justin Kuczynski, Kevin Tritz, Martin Thoma, Matthew Newville, Matthias Kümmerer, Maximilian Bolingbroke, Michael Tartre, Mikhail Pak, Nathaniel J. Smith, Nikolai Nowaczyk, Nikolay Shebanov, Oleksandr Pavlyk, Per A. Brodtkorb, Perry Lee, Robert T. McGibbon, Roman Feldbauer, Sam Lewis, Sam Tygier, Scott Sievert, Sebastiano Vigna, Stefan Peterson, Surhud More, Tadeusz Pudlik, Takuya Oshima, Thomas J. Pingel, Thomas P. Robitaille, Thomas Spura, Thouis R. Jones, Tim Cera, Tim Leslie, Tiziano Zito, Tom Krauss, Utkarsh Upadhyay, Yaroslav O. Halchenko, and Yoshiki Vázquez-Baeza. SciPy 1.0: fundamental algorithms for scientific computing in Python. *Nature Methods*, 17(3):261–272, 2020. [6](#)
- [43] Matthew D. Walker, Andrew J. Morgan, Kevin M. Bradley, and Daniel R. McGowan. Data-Driven Respiratory Gating Outperforms Device-Based Gating for Clinical ^{18}F -FDG PET/CT. *Journal of Nuclear Medicine*, 61(11):1678–1683, 2020. [2](#)
- [44] Simon M. Walker, Daniel A. Schwyn, Rajmund Mokso, Martina Wicklein, Tonya Müller, Michael Doube, Marco Stampanoni, Holger G. Krapp, and Graham K. Taylor. In Vivo Time-Resolved Microtomography Reveals the Mechanics of the Blowfly Flight Motor. *PLoS Biology*, 12(3): e1001823, 2014. [2](#)
- [45] Matthias K. Werner, J. Anthony Parker, Gerald M. Kolodny, Jeffrey R. English, and Matthew R. Palmer. Respiratory Gating Enhances Imaging of Pulmonary Nodules and Measurement of Tracer Uptake in FDG PET/CT. *American Journal of Roentgenology*, 193(6):1640–1645, 2009. [1](#)
- [46] Philip J. Withers, Charles Bouman, Simone Carmignato, Veerle Cnudde, David Grimaldi, Charlotte K. Hagen, Eric Maire, Marena Manley, Anton Du Plessis, and Stuart R. Stock. X-ray computed tomography. *Nature Reviews Methods Primers*, 1(1):18, 2021. [1](#)
- [47] Yanlin Wu, Hidekazu Takano, and Atsushi Momose. Time-resolved x-ray stroboscopic phase tomography using Talbot interferometer for dynamic deformation measurements. *Review of Scientific Instruments*, 92(4):043702, 2021. [1](#), [2](#)
- [48] Qi Zhang, Duo Zhang, and Greta S. P. Mok. Comparison of different attenuation correction methods for dual gating myocardial perfusion spect/ct. *IEEE Transactions on Radiation and Plasma Medical Sciences*, 3(5):565–571, 2019. [2](#)
- [49] Yongbin Zhang, Jinzhong Yang, Lifei Zhang, Laurence E. Court, Peter A. Balter, and Lei Dong. Modeling respiratory motion for reducing motion artifacts in 4D CT images. *Medical Physics*, 40(4):041716, 2013. [1](#)

Analytical Reconstruction of Periodically Deformed Objects in Time-resolved CT

Supplementary Material

7. More results

7.1. Video comparison

The supplementary video compares the reconstruction results of the gating-based method and our approaches, covering the entire period of the sound.

More videos are also available on the YouTube channel [@PeriodRecon](#).

7.2. Example of low-dose reconstruction

Here, we present an example of low-dose reconstruction using fewer projection angles. For the gating-based method, we divide all projections into 20 bins, with each bin containing 1000 projection angles, resulting in a total of 20 000 projection angles. In our approach, we down-sample the projections by a factor of 4 in terms of exposure, reducing the total number of projection angles to 5000.

As shown in Fig. 11 and Tab. 2, despite using only a quarter of the projections, our method achieves the same reconstruction quality as the gating-based method.

Table 2. Noise level comparison. The noise is sampled from the regions marked with blue boxes in Fig. 11. The standard deviation (STD) values of the intensities are listed in this table.

Row	Gating	LIA	FS
1	1.47×10^{-3}	1.07×10^{-3}	1.47×10^{-3}
2	1.45×10^{-3}	1.02×10^{-3}	1.45×10^{-3}
3	1.45×10^{-3}	1.02×10^{-3}	1.43×10^{-3}
4	1.46×10^{-3}	1.03×10^{-3}	1.45×10^{-3}
5	1.47×10^{-3}	1.03×10^{-3}	1.46×10^{-3}
6	1.44×10^{-3}	1.02×10^{-3}	1.42×10^{-3}

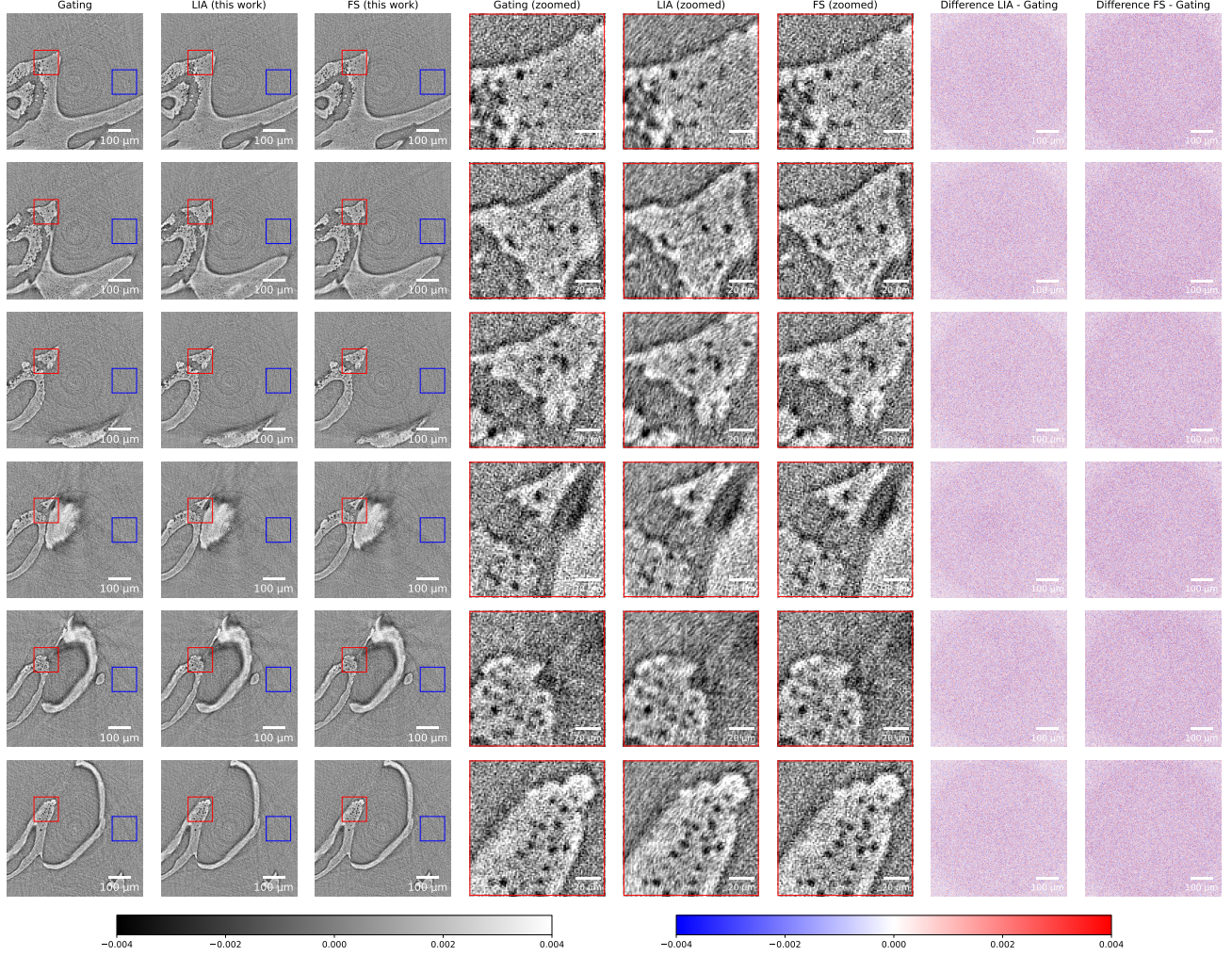


Figure 11. Reconstruction quality comparison for the sound phase of 9 degrees. The figure compares the reconstructed slices obtained using the gating-based method (first column) and our methods (second and third columns). The fourth to the sixth columns are the blow-ups of the red boxes regions in the first three columns, respectively. The last two columns show the intensity differences between the images in the first three columns. For our methods, we utilize 5000 projections to do the reconstruction while 20 000 totally for the gating-base one.